

# DEEP IMAGING OF AXJ2019+112: THE LUMINOSITY OF A “DARK CLUSTER”<sup>1</sup>

Narciso Benítez<sup>2</sup>, Tom Broadhurst<sup>2</sup>, Piero Rosati<sup>3</sup>, Fred Courbin<sup>4</sup>, Gordon Squires<sup>5</sup>, Chris Lidman<sup>3</sup>, Pierre Magain<sup>4,6</sup>

## ABSTRACT

We detect a distant cluster of galaxies centered on the QSO lens and luminous X-ray source AXJ2019+112, a.k.a. “The Dark Cluster” (Hattori et al 1997). Using deep  $V, I$  Keck images and wide-field  $K_s$  imaging from the NTT, a tight red sequence of galaxies is identified within a radius of  $0.2h^{-1}$  Mpc of the known  $z = 1.01$  elliptical lensing galaxy. The sequence, which includes the central elliptical galaxy, has a slope in good agreement with the model predictions of Kodama et al (1998) for  $z \sim 1$ . We estimate the integrated rest-frame luminosity of the cluster to be  $L_V \geq 3.2 \times 10^{11} h^{-2} L_\odot$  (after accounting for significant extinction at the low latitude of this field), an order of magnitude higher than previous estimates. The central region of the cluster is deconvolved using the technique of Magain, Courbin & Sohy (1998), revealing a thick central arc coincident with an extended radio source. All the observed lensing features are readily explained by differential magnification of a radio loud AGN by a shallow elliptical potential. The QSO must lie just outside the diamond caustic, producing two images, and the arc is a highly magnified image formed from a region close to the center of the host galaxy, projecting inside the caustic. The mass-to-light ratio within an aperture of  $0.4h^{-1}$  Mpc is  $M_x/L_V = 224_{-78}^{+112} h(M/L_V)_\odot$ , using the X-ray temperature. The strong lens model yields a compatible value,

---

<sup>1</sup>Based on observations collected at the European Southern Observatory, La Silla, Chile, proposal number 61.A-0676

<sup>2</sup>Astronomy Department, UC Berkeley, 601 Campbell Hall, Berkeley, CA

<sup>3</sup>European Southern Observatory, D-85748, Garching, Germany

<sup>4</sup>Institut d’Astrophysique et de Géophysique, Université de Liège, 5, Avenue de Cointe, B-4000 Liège, Belgium and URA 173 CNRS-DAEC, Observatoire de Paris, F-92195 Meudon Principal CEDEX, France

<sup>5</sup>Center for Particle Astrophysics, UC Berkeley, 301 Le Conte Hall, Berkeley, CA

<sup>6</sup>Also Maître de Recherches au FNRS

$M/L_V = 372_{-94}^{+94}h(M/L_V)_\odot$ , whereas an independent weak lensing analysis sets an upper limit of  $M/L_V < 520h(M/L_V)_\odot$ , typical of massive clusters.

*Subject headings:* Gravitational lensing; Galaxy clusters; Dark matter

## 1. Introduction

Hattori et al. (1997; hereafter H97) have recently shown that the well studied QSO lens Q2016+112 is coincident with an extended X-ray source of hot bremsstrahlung radiation, AXJ2019+112. The association is based on good positional agreement with high resolution ROSAT HRI data and also by a plausible consistency in redshift between the central lensing galaxy at  $z = 1.01$  (Schneider et al. 1985) and an X-ray emission line, interpreted as FeXXV at  $z \approx 1$ . The detection of enriched gas at high redshift, comparable in iron abundance to local clusters, is puzzling and exacerbated by the absence of any obvious cluster of galaxies at this location (Schneider et al 1985, Langston, Fischer & Aspin 1991), to provide a potential means of IGM enrichment.

Other claims of “dark” cluster sized objects have been made on the basis of SZ-decrements (Jones et al. 1997, Richards et al. 1997) indicating cluster sized plasma concentrations at redshifts in excess of unity (Bartlett et al. 1998). However, a follow-up deep X-ray observation of PC1643+4631 limits any such plasma to an unreasonably high redshift (Kneissl, Sunyaev & White 1998), and there is no evidence for an excess of galaxies toward that direction (Ferrerias, Benítez, & Martínez-Gonzalez 1998, Saunders et al. 1997). Therefore, confirmation for the existence of these high redshift ‘dark’ clusters should await improved radio data.

In contrast, fairly conventional looking X-ray selected clusters have now been identified at redshifts as high as  $z = 1.27$  (Stanford et al. 1998, Rosati et al. 1998b). These clusters have obvious E/SO color sequences, identified by optical-IR color and, depending on their masses, are hard to account for in the standard account of structure formation with high  $\Omega$  (Bahcall & Fan 1998, Eke et al. 1998). On purely empirical grounds, the existence of X-ray luminous clusters at  $z \simeq 1$  is not surprising. Recently completed deep X-ray surveys show no evidence of a decline in the space density of  $L_x \sim L_x^*$  X-ray selected clusters over a wide redshift range,  $0.2 < z < 0.8$  (Rosati et al. 1998a).

Here we show that the low galactic latitude of AXJ2019+112 ( $|b| = 13.6$ ) significantly impedes the detection of faint galaxies in this field, due to the extended halos of numerous bright stars and significant Galactic extinction. In §3 we analyze very deep, 0'6 images

taken with the Low Resolution Imaging Spectrometer (LRIS) on Keck II (§2), and identify a sequence of red galaxies in  $V - I$ , centered on the lens. This identification is bolstered by deep  $K_s$ –band images, obtained using the new infrared spectrograph and imaging camera SOFI on the NTT. In §4 we reanalyze the archived ROSAT HRI X-ray observations of this field, possibly resolving three significant sources of emission, one of which is marginally extended and coincident with the cluster, leading to a significant revision of the published X-ray luminosity. In §5 we provide an independent upper limit to the M/L for the cluster from a weak lensing analysis using the Keck images. In §6 we deconvolve the central region of the field, finding an arc around the brightest cluster elliptical, and finally in §7 we use this and a simple lens model to reconcile the many radio sources and optical/IR lensing features. In §8 we summarize the main results and conclusions.

Throughout this paper we assume  $\Omega_0 = 1, \Lambda = 0, h = H_0/(100 \text{ Mpc km s}^{-1})$ .

## 2. Optical and Near-IR Imaging and photometry

Deep  $V$  and  $I$  images were obtained with LRIS at the KeckII telescope on the night of 1997 June 29th. The seeing was good,  $0''.62$  in the  $I$ –band and  $0''.65$  in  $V$ . The images cover an area of size  $5'.5 \times 7'.5$ .

The optical images were debiased and flattened with dome flats and illumination corrected using standard procedures. The  $I$ –band images are badly affected by fringing. This was accurately removed by generating a fringing pattern from combined observations of other fields taken on the same night. The resulting  $V$  and  $I$ –band images were aligned with a small correction for a relative distortion across the field, requiring a third order polynomial. The final, averaged images have total exposure times of 1480s in  $I$  and 1980s in  $V$  with a scale of  $0''.215/\text{pixel}$  and represent the highest quality optical images of this field to date. Calibration was obtained in July 1998 by observing the field and several Landolt standards with LRIS and the same filter. The magnitude zero point uncertainties are 0.03 in both the  $I$  and  $V$ –bands, and no appreciable color term was detected. Due to the low galactic latitude of the field ( $b = -13.6$ ), the error in the absolute zero point is dominated by the uncertainty in the value of the galactic extinction. Burstein & Heiles 1982 give an extinction of  $A(B) = 0.98$  at our position, corresponding to  $A(V) \approx 0.74$  and  $A(I) \approx 0.44$ . The more direct and higher resolution estimation of Schlegel, Finkbeiner, & Davis 1998, based on an IRAS/DIRBE map, gives  $A(B) = 0.81 \pm 0.12$ , in marginal agreement with Burstein & Heiles 1982. We adopt the extinction of Schlegel, Finkbeiner, & Davis 1998, which yields  $A(V) = 0.67 \pm 0.10$ ,  $A(I) = 0.36 \pm 0.06$  and  $A(K_s) = 0.08 \pm 0.01$ . Therefore, the total zero point uncertainties are 0.1 in  $V$ , 0.07 in  $I$  and 0.06 in  $V - I$ . The  $5\sigma$  limiting

magnitudes within an aperture of  $1''.5$  are  $I = 25.32$  and  $V = 26.65$ .

In addition wide field  $K_s$ –band images were acquired on the night of 1998 July 10th, with SOFI, a new wide field infra–red imager and spectrograph on the ESO NTT (Moorwood, Cuby & Lidman 1998). SOFI uses a Rockwell 1024 square Hg: Cd:Te device, which gives a field size of  $5' \times 5'$  in the large field imaging mode. The pixel scale is  $0''.288$ .

In total, 90 separate images of MG2016 were taken with the  $K_s$  filter. Each image is itself a stack of six short integrations, each of 10 seconds. The telescope was offset in a random manner by  $40''$  or less between each stack to help in generating an accurate sky background measurement over the full field.

The data was reduced by first subtracting the bias with an averaged dark frame, and then dividing out the variations in pixel sensitivity with normalized dome flats. The sky was estimated for each image individually by constructing a running mean of the adjacent 10 dithered exposures, with suitable clipping to remove objects. The images were then registered and combined. The intensity of the sky during the observations ranged between 13 and  $13.2 \text{ mag/arcsec}^2$ .

The final  $K_s$  image is the average of 68 images with a resulting seeing of  $\approx 0''.7$  and a total exposure time of 4080s. This image excludes frames with resolution lower than  $0''.9$  comprising  $\approx 25\%$  of the total. The conditions at the time of the observations were photometric. The magnitude scale was determined by observing four standards from the list of Persson et al. (1998). The scatter between the standards is 0.015 magnitudes. The  $5\sigma$  detection within a  $1''.5$  aperture is  $K_S = 21.25$ .

### 3. Reduction

Due to the low galactic latitude of the field, the star density is very high, so that most of the area of the field is covered by the extended haloes of the brightest stars, especially in the  $I$ –band (Fig 1a). We find that the best approach to dealing with this problem is to generate a “halo” pattern by setting the central parts of the stars and the saturation spikes to the average background level and then applying a broad,  $11'' \times 11''$ , median filter to the image. The pattern thus obtained is subtracted from the original frame and the resulting image used for object detection. In a final step, all the bright cores of the stars, including their saturated trails, are masked out. The initial and final, ‘de-haloed’  $I$ –band images are shown for comparison in Fig 1a,b.

The smoothing and masking affects the photometry of bright extended objects, but

Fig. 1.—  $I$ -band image of the field around Q2016+112 before (a) and after (b) the halo removing procedure. The white circle shows a  $0.4h^{-1}$  Mpc diameter aperture ( $47''$ ) at  $z = 1$  centered on galaxy  $D$

on average it does not affect the fainter ones. This is established using similarly deep but much higher latitude Keck  $I$ -band observations of a control image PSR 1640+22 field (Smail et al. 1995). This field was scaled so that the background noise level was the same as in our Q2016+112  $I$  image. Then we add it to all the haloes and bright objects from our cluster field, i.e. the difference between Fig 1a and Fig 1b. In this way, a test image is created with the same ‘halo’ characteristics as Fig 1a but with a known ‘uncontaminated’ galaxy background for performing tests. We then apply exactly the same halo removing procedure described above. In establishing the errors introduced by the haloes and the improvement from the halo removal procedure we make use of the detection software SExtractor (Bertin & Arnouts 1996) to produce three catalogs. Firstly we create a catalog of the photometric properties of the test field before any changes are made (catalog O). Secondly a catalog is created for the halo contaminated control (catalog H) field by adding the halos from the cluster frame to the control field, and finally a catalog (dH) is generated for the halo subtracted control field after applying our correction for the haloes in exactly the same way as for the cluster field.

Comparing the test field catalog (O) with those of the halo affected images of this same field (H and dH) allows a reliable empirical estimate of the effect of the haloes on the magnitude estimates and also measures the degree of improvement achieved by our halo removal procedure. The comparison of the magnitude differences between catalogs (H) and (O), and catalog (dH) and (O) shows that the presence of numerous stars with extended haloes distorts the estimation of the background, and is a stronger source of photometric noise than any additional uncertainty in eliminating the haloes. These tests also allow us to estimate the percentage of ‘useful surface’ recovered with our procedure. On the image obtained after adding the haloes we only detect between 35%(at  $I \approx 20$ ) and 25% at ( $I \approx 25.5$ ) of the objects which were initially present on the PSR 1640+22 image. After the halo removing procedure, we recover respectively between 30%( $I \approx 20$ ) and 45%( $I \approx 25.5$ ) of the same objects. The maximum possible detection efficiency (found by excluding from the PSR 1640+22 original frame all objects which have at least one pixel in the masked areas) is 44%(at  $I \approx 20$ ) and 72%( $I \approx 25.5$ ), in the last case approaching the percentage of ‘non-masked’ area, 74.5%. This means that apart from obtaining slightly more reliable magnitudes, the followed procedure increases by  $\approx 80\%$  the useful surface for detecting faint objects. Fortunately, as can be seen in Fig 1, the central region containing the cluster is one of the least affected by haloes. But in the rest of the image, in particular areas close

to bright haloes, the tests show that apart from the standard photometric errors there is an increased random error in the magnitude estimates of  $\approx 0.2$  in the  $I$ –band magnitude compared to the ‘halo-free’ image.

The detection and classification of objects in the  $V, I$  and  $K$  images is made using SExtractor v2.0 (Bertin & Arnouts 1996). This software smooths the images with a gaussian of size close to the seeing width, and then locates peaks above a given threshold. To obtain accurate colors we use the  $I$ –band image for detection and use the apertures obtained for each of image to perform the  $V$  and  $K_S$ –band photometry. These matched apertures are ideal given the very similar seeing for all 3 passbands.

It was found that somewhat different definitions of magnitudes are required for bright and faint galaxies for best results, due to the approach of all faint galaxies to the seeing profile. For the bright galaxies we adopt the SExtractor Kron-like ‘automatic’ magnitudes  $m_{au}$ , with a  $k$  parameter of 2.5. These apertures encompass  $\approx 95\%$  of the total object magnitudes (Bertin 1998). To prevent the magnitudes from being affected by crowding, SExtractor masks the pixels belonging to neighboring objects and replaces their values by those of pixels lying symmetric opposed to the source center. For faint objects ( $I > 23.5$ ), we measure the magnitude within a fixed aperture of  $1''.5$  and correct it to the automatic magnitude assuming that faint objects have roughly stellar profiles. This was established by stacking together many faint objects. The corresponding corrections are 0.14 in the  $I$ –band and 0.21 in the  $V$  band.

SExtractor assigns to each object a value of the parameter “class-star”, which ranges from 0 to 1. If the seeing FWHM is well determined, stars obtain values of this parameter close to 1, whereas for extended objects it tends to be close to 0. The classification, performed using the  $I$ –band images, works satisfactorily for objects with  $I \lesssim 24.7$ , which corresponds to a detection with a  $S/N \gtrsim 9$  within a  $1''.5$  aperture. At fainter magnitudes, SExtractor assigns similar values of the “class-star” parameter  $\approx 0.4 - 0.5$  to all objects. One of our main concerns is to avoid the contamination of our galaxy sample by stars, specially some of them, e.g. disk M dwarfs, would have the same colors as early-type galaxies at the cluster redshift. This is achieved by excluding those objects with  $I > 24.7$  and imposing a very conservative threshold in the “class-star” parameter, 0.25. The  $V - I$  vs.  $I$  plots of the central region around the lens and the rest of the frame are shown in Fig 2. Objects with  $V$  fainter than  $V = 27.0$ , corresponding to a  $3.5\sigma$  detection within a  $1''.5$  aperture, have been excluded. Fig 4 shows the  $V - I$  vs  $I - K$  for all the galaxies in the field. Objects fainter than  $K_S = 21.60$ , corresponding to a  $3.5\sigma$  detection within a  $1''.5$  aperture, have been excluded.

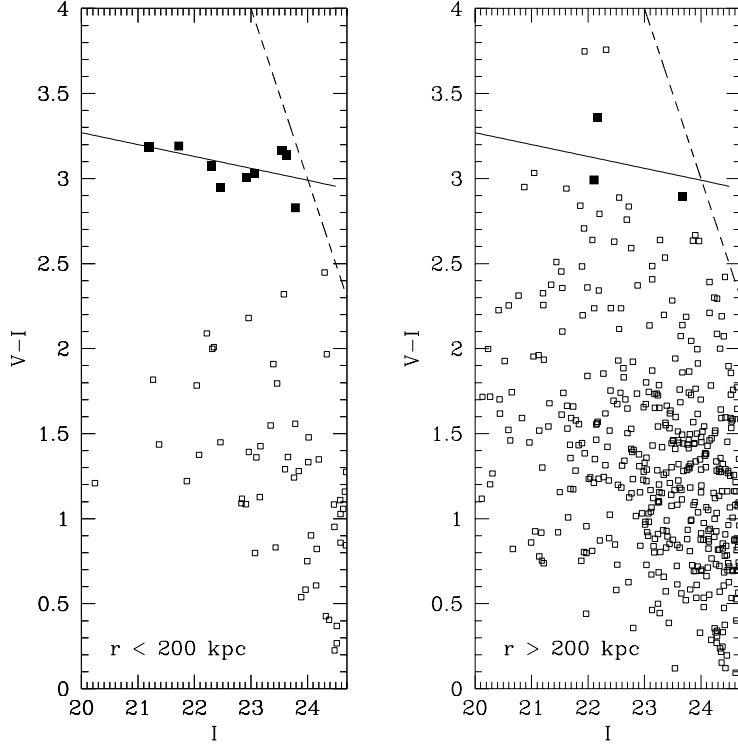


Fig. 2.— Color magnitude diagram for the central  $0.4h^{-1}\text{Mpc}$  region around Q2016+112 (left) and for the rest of the frame. The filled squares indicate the positions of the ‘red sequence’ galaxies; objects compatible with having  $V - I = 3.19 - 0.07 \times (I - 21.20)$  within errors

#### 4. The galaxy cluster

Recent work (Stanford, Eisenhardt & Dickinson 1998, Kodama et al. 1998) has shown that cluster ‘red sequences’, the locus in the color–magnitude diagrams of the cluster early type galaxies, represent a remarkably stable feature which is detected up to  $z > 1$  redshifts (e.g. on the  $z = 1.2$  cluster around 3C324, Dickinson 1995). The red sequence is an excellent marker of the presence of a massive cluster, since galaxies with the colors and magnitudes of cluster early types are scarce among the general field population.

To examine the data for evidence of a cluster sequence, we have divided the frame into two regions, one corresponding to a  $0.4h^{-1}\text{Mpc}$  circular aperture at  $z = 1.01$ , centered on the luminous galaxy *D* (Fig 9b), and an outer region covering the rest of the image. Using the magnitude of galaxy *D* as its zero-point ( $I = 21.20$ , measured using the deconvolved

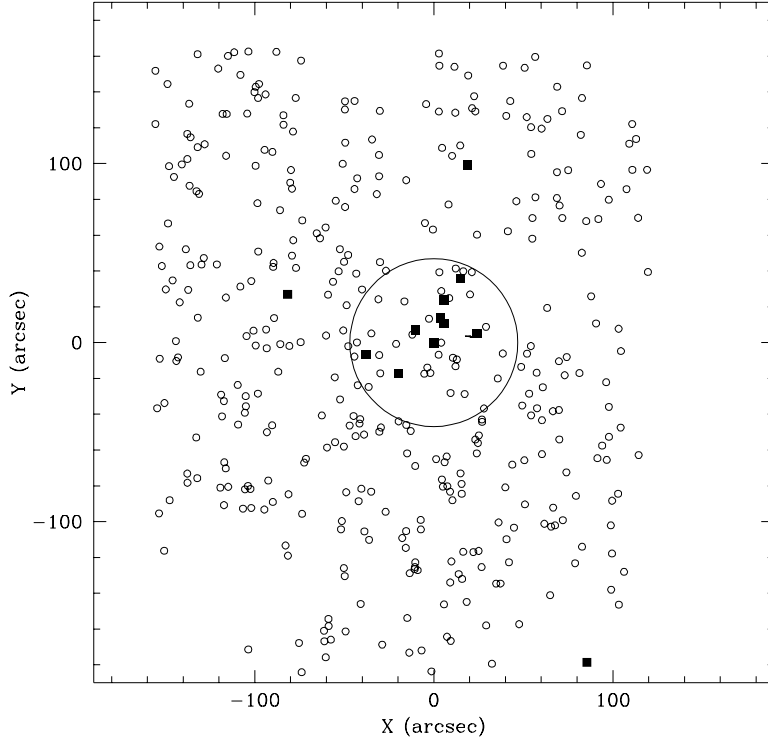


Fig. 3.— Spatial distribution of the cluster early type candidates, represented by filled squares. The empty squares represent the stars detected on the frame. The circle corresponds to a  $0.2h^{-1}$  Mpc radius at  $z=1$

images obtained in Sec 6), and adopting a slope of 0.07 at  $z = 1.01$  (Kodama et al. 1998), the early-type sequence of such a cluster should lie at  $V - I = 3.19 - 0.07(I - 21.20)$ . Fig 3 shows the positions of the galaxies with magnitudes compatible within their observational error with this relationship, and those of all the stars in the frame (objects with class-star higher than 0.95), independently of their color. It is obvious from this figure that a red sequence of galaxies is clustered around  $D$  and also that galaxy  $D$  lies on this sequence. The central region has 8 such candidates (excluding galaxy  $D$ ), whereas there are only other 3 such galaxies on the rest of the frame. The central circle contains 54 stars against 390 detected in all the frame, i.e. the central region comprises only 13.8% of the ‘useful’ surface in the frame. Thus, there is a factor  $\approx 20$  overdensity of red galaxies in the central 0.4 Mpc, clear evidence of the existence of a galaxy cluster. A rough estimation of the significance of this result may be performed using a binomial distribution. The probability of having  $k$  galaxies out of a total of  $n$  within a region containing a fraction  $p$  of the total surface is represented by  $p(n, k) = C_n^k p^k (1 - p)^{n-k}$ . With  $n = 11$ ,  $k = 8$  and  $p = 0.138$ , we



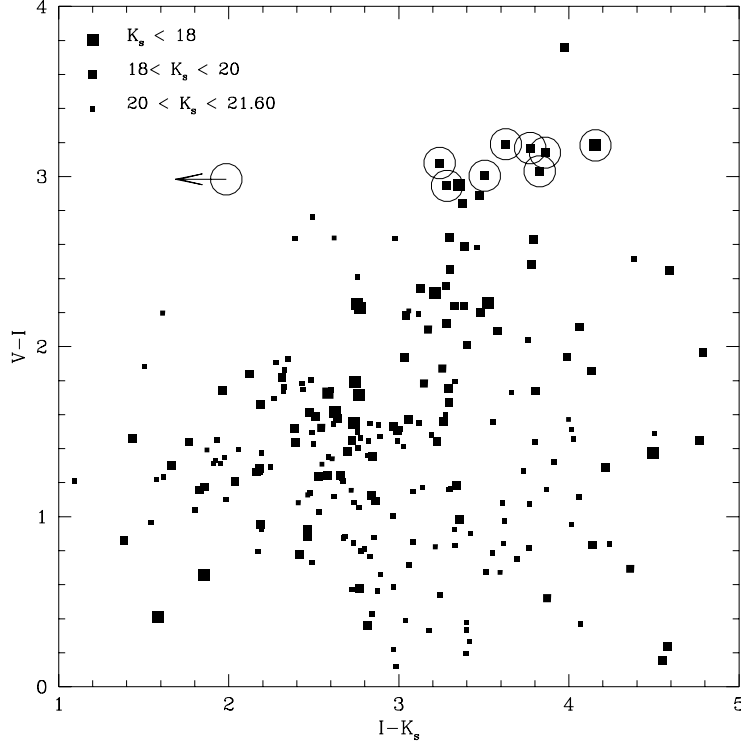


Fig. 4.—  $V - I$  vs  $I - K$  plot for all the galaxies in the field. The objects identified as cluster members on the basis of the  $V - I$ ,  $I$  plot are circled. The arrow indicates an upper limit

find  $p(11, 8) = 1.4 \times 10^{-5}$ , corresponding to a confidence level of  $> 99.998\%$ . Fig 4 shows that all but one of the cluster member candidates selected on the basis of the  $V - I$ ,  $I$  are also very red in  $I - K_s$ . This further supports that these galaxies are physically associated. Independently, in addition to galaxy *D*, two of our sequence galaxies have spectroscopic redshifts, and both are claimed to lie at  $z = 1.0$  (Kneib et al. 1998).

In the remainder of this paper, the galaxies listed in table 1 (except the one which is not detected in the  $K$ -band) will be considered cluster members. To estimate their absolute magnitudes  $M_V$ , we use a  $k$ -correction of 3.5 at  $z = 1.01$  for evolved ellipticals (Poggianti 1997), and a distance modulus of 42.75. Galaxy *D* has a de-reddened luminosity of  $L_V^D = 4.16 \pm 0.21 \times 10^{10} h^{-2} L_\odot$ , and the total luminosity of the detected cluster candidates is  $L_V = 1.33 \pm 0.08 \times 10^{11} h^{-2} L_\odot$ . Our detection limit of  $V = 27$  corresponds to  $M_V = -19.25$ , so to compare this luminosity with the results of Smail et al. 1997 (hereafter S97), we correct it by integrating a Schechter function up to  $M_V = -18.5$ , using  $\alpha = -1.25$  and  $M_V^* = -20.75 + 5 \log h$ , measured by S97 at  $< z = 0.55 >$ . The correction amounts to

20% of the total light, and it is quite robust with respect to the exact value of  $M_V^*$ , ranging from 30% for  $M_V^* = -20.30$  to 10% for  $M_V^* = -21.60$ . The adopted total luminosity for the cluster early type population is thus  $L_V^E = 1.6 \pm 0.2 \times 10^{11} h^{-2} L_\odot$ . In the cluster sample of S97 the early types contain typically 50% of the total cluster light. Therefore, the total luminosity of the ‘dark’ cluster would be  $L_V^{\text{all}} \approx 3.2 \times 10^{11} h^{-2} L_\odot$ . This value probably underestimates the cluster luminosity, as the fraction of cluster galaxies with star formation, and therefore bluer than the red cluster sequence, is likely to be higher at  $z = 1$  than at  $z \lesssim 0.5$ .

H97 quote a value of  $L_B = 2.75 \times 10^{10} h^{-2} L_B^\odot$  for galaxy  $D$ . As no other obvious cluster galaxy candidates were known, they adopted that value as the total luminosity. Assuming a color of  $B_J - V \approx 0.6$  for an elliptical at redshift  $z = 1$ , their value of  $L_B$  would correspond to  $L_V \approx 3 \times 10^{10} h^{-1} L_\odot$ , an order of magnitude lower than our estimate of the total cluster light.

## 5. X-ray analysis

We have reanalyzed the ROSAT-HRI archival observations to examine the spatial relationship between the optical and X-ray emission. The HRI dataset consists of three separate pointings with ROSAT ID: rh800811n00, rh800811a01, rh800811a02 with a total exposure time of 79 ksec. The X-ray photon files have been processed with standard IRAF-PROS routines filtering out time intervals with high background rate. The resulting coadded image with  $4''$  pixel size has an effective exposure time of 56.0 ksec, mostly contributed from the A01 and A02 observations. The astrometrical accuracy is found to be better than  $5''$  using 2 bright X-ray sources coincident with bright stars. A faint source at  $4\sigma$  level is detected within  $3''$  of the position of the elliptical  $D$ . A second source ( $\sim 4.5\sigma$ ) is found  $30''$  NE. The latter seems to be missing in the original analysis by H97. However, inspection of several images obtained by splitting the observation in two time intervals reveal variations in the flux of this source, suggesting that it might be either variable or spurious, whereas the central source shows a consistent flux. Furthermore, the elliptical morphology of the central X-ray source is present in two independent pointings, suggesting that it is not an artifact of the background noise. This central source is the natural X-ray counterpart of the optical cluster and is likely coincident with the ASCA source of H97. The central 3 arcmin of the HRI field are shown in Fig 5. Corresponding X-ray contours are overlaid on the  $VIK$  color image of the field in Fig 6.

We find  $17 \pm 9$  net counts, or a count rate of  $(3.0 \pm 1.6) \times 10^{-4}$  cts s $^{-1}$  in the central source within a circle of  $20''$  radius ( $\simeq 85 h^{-1}$  kpc at  $z = 1$ ). The flux within a circle of

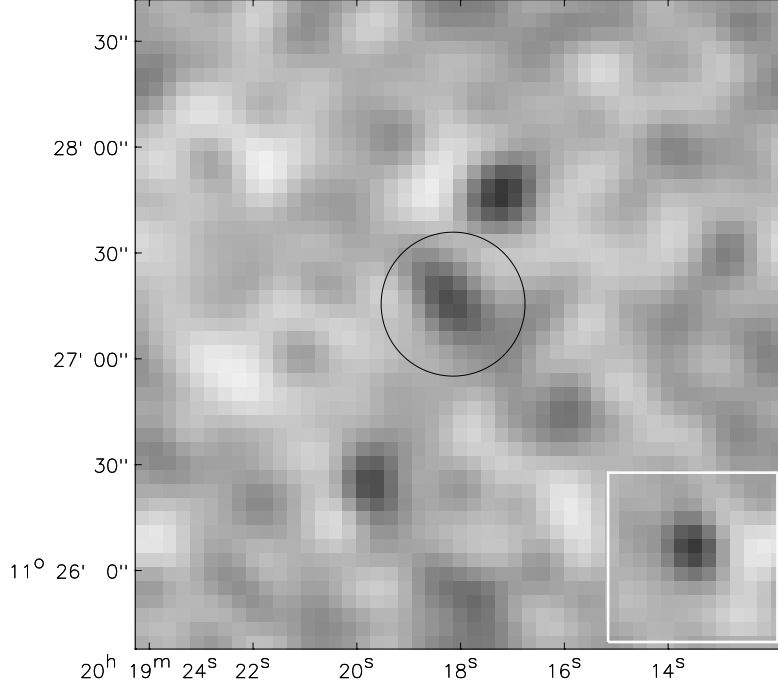


Fig. 5.— Central region of the ROSAT-HRI field smoothed with a gaussian filter with  $\sigma = 6''$  to match the resolution of the HRI data. The source in the lower right box is a simulated point-like source with the same flux encircled by the central source, to show the difficulty of resolving the central X-ray emission.

$1'$  falls short of the H97 estimate by a factor of two. Using a galactic hydrogen column density of  $N_H = 1.5 \times 10^{21} \text{ cm}^{-2}$  and a Raymond-Smith spectrum with  $T \simeq 8 \text{ keV}$ , as measured by H97, the program PIMMS for the HRI yields that 1 cts/s is equivalent to an unabsorbed flux of  $6.06 \times 10^{-11} \text{ erg cm}^{-2} \text{ s}^{-1}$  in the 0.1 – 2.0 keV band. The flux of the central source is  $F_x(< 20'') = 1.8 \times 10^{-14} \text{ erg cm}^{-2} \text{ s}^{-1}$ , or an X-ray luminosity at  $z = 1$ ,  $L_x(< 20'') = 1.1 \times 10^{44} \text{ erg s}^{-1}$  in the observed 0.1-2 keV band. The K-correction amounts to a factor 1.4, whereas the conversion factor for the 2-10 keV band is  $\sim 1.6$ . Therefore,  $L_s(< 20'') = (1.1/1.4 \times 1.6) = 1.3 \times 10^{44} \text{ erg s}^{-1}$  in the 2-10 keV rest frame band. This value is a factor 3-4 lower than the estimate by H97, even with extrapolation of the flux out to  $1'$  using their assumed surface brightness profile. Given the low signal-to-noise of the central source, it is not possible to assess its angular extent. This is shown visually in Fig 5, where the HRI PSF has been used to simulate a source of 17 counts and added to the central region. The comparison between the surface brightness profiles of the central object

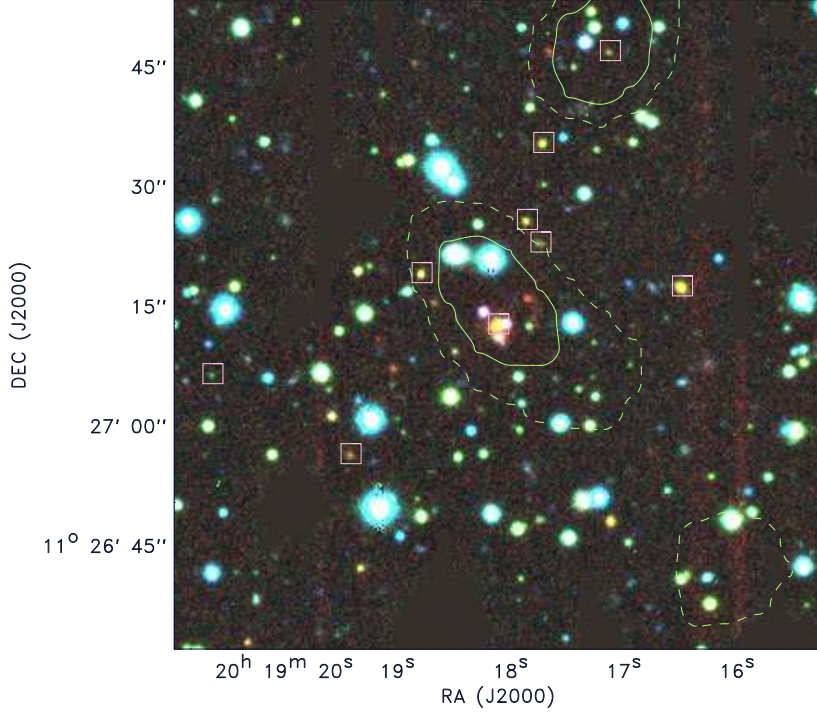


Fig. 6.— ROSAT-HRI contours overlaid on the optical-IR (*VIK*) image of the MG2016 field. The contours are at 2 (dashed) and 3  $\sigma$  levels (smoothing gaussian scale  $\sigma = 8''$ ). The boxed objects the cluster galaxies candidates belonging to the red  $V - I$  sequence listed in Table 1. This figure demonstrates that the red galaxy overdensity is spatially coincident with the central X-ray emission.

and the point-like (noise-less) source is shown in Fig 7, although at these low S/N levels, profile fitting is rather meaningless. The spatial analysis of H97 suggested an extended central source. This might be due to the large smoothing scale (FWHM=  $35''$ ) used by those authors or to a higher background of our combined X-ray image.

The fact that the X-ray emission of a cluster at  $z = 1$  is unresolved with the HRI is not surprising, given the severe surface brightness dimming at this redshift (Rosati et al. 1998a). However, we cannot rule out a significant contribution to the X-ray emission from the two lensed QSO images. Therefore, the aforementioned X-ray luminosity should be considered an upper limit. Improved observations, ideally spatially resolved spectroscopy, should help to clarify the relation between the hot thermal spectrum observed by ASCA, with its low spatial resolution, and the patchy nature of the much better resolved

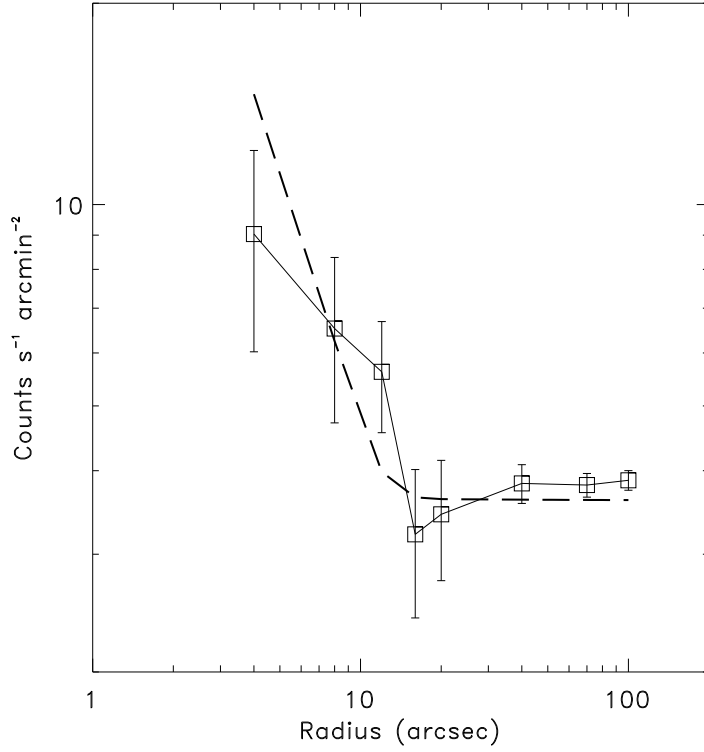


Fig. 7.— X-ray surface brightness profile of the central HRI source. The HRI noiseless PSF for a source of the same flux is superimposed (dashed line). The background is equal to  $\sim 3.6$  counts  $\text{s}^{-1} \text{ arcmin}^{-2}$ . The possibility that this emission is unresolved is hard to exclude.

#### ROSAT-HRI map.

Assuming that the cluster is isothermal and in hydrostatic equilibrium, Hattori et. al. estimate the gravitational mass within a radius of  $0.5h^{-1} \text{ Mpc}$  to be  $M = 1.8_{-0.6}^{+0.9} \times 10^{14} h^{-1} M_{\odot}$ , where the errors represent the uncertainty in the cluster temperature determination  $kT = 8.6_{-3.0}^{+4.2} \text{ keV}$ . Assuming  $M \propto r$ , the mass inside a  $0.2h^{-1} \text{ Mpc}$  radius would be  $M_x = 7.2_{-2.5}^{+3.5} \times 10^{13} h^{-1} M_{\odot}$ . This gives a mass to light ratio for AXJ2019+112 of  $M_x/L_V^E = 448_{-153}^{+224} h(M/L_V)_{\odot}$  and  $M/L_V^{all} = 224_{-78}^{+112} h(M/L_V)_{\odot}$ , compatible with the median values of  $z \lesssim 0.5$  clusters (S97):  $M/L_V^E = 330_{-110}^{+210} h(M/L_V)_{\odot}$  and  $M/L_V^{all} = 180_{-80}^{+140} h(M/L_V)_{\odot}$ .

## 6. Weak lensing Analysis

The observations are of sufficient depth and resolution to allow a useful weak lensing analysis. The procedure for measuring the lensing signal is standard, and follows that employed in other cluster lensing studies (e.g., Squires et al. 1996). Object finding and analysis employed the IMCAT software developed by N. Kaiser (Kaiser, Squires & Broadhurst 1995 – KSB). Correction for psf anisotropy, and circularization due to seeing was made with the standard formalism of KSB and Luppino/Kaiser (1997), with corrections noted in Hoekstra et al. (1998). Correction for these systematics is very robust, due to the very regular psf in the final coadded images, and the overabundance of stars in this field. The residual ellipticity in the corrected star catalog is less than 0.1% over the full field and so residual systematic shape distortion in the galaxy catalogs is completely negligible.

Using the standard unbiased inversion algorithm (e.g., Kaiser & Squires 1994; Squires & Kaiser 1996), and the  $\zeta$ -statistic, we determine the cluster surface density from the corrected galaxy shape measurements. For  $I < 25$  we find a *null* detection of the cluster mass distribution, both in a 2D mass map, and in the radially averaged mass profile.

This null detection allows us to place an interesting upper limit on the cluster mass, albeit in a model dependent fashion. For example, assuming the cluster follows a isothermal profile,  $\rho(r) = \sigma_v^2 / 2\pi G r^2$ , where  $\sigma_v$  is the line of sight velocity dispersion, our data are of sufficient depth to detect the signal from a 1000 km/s singular isothermal sphere (SIS) cluster at the  $3\sigma$  level at  $r = 1'$  and a  $2\sigma$  level at  $r = 2'$ , for  $\beta = 0.2$ . In terms of mass, for a cluster with  $\sigma = 1300 \text{ km s}^{-1}$  (typical of clusters with  $T_x \approx 8.5 \text{ keV}$ ) this model yields

$$M_{3D} < 1.6 \times 10^{14} \left( \frac{\sigma}{1300 \text{ km s}^{-1}} \right)^2 \left( \frac{\beta}{0.2} \right)^{-1} \left( \frac{r}{200 h^{-1} \text{ kpc}} \right) h^{-1} M_{\odot} \quad (1)$$

where  $\beta$  describes the average relative distance between the lens and the source galaxies. For  $I < 25$  and for plausible cosmologies and star formation models,  $\beta$ , ranges between 0.16 and 0.23, so the above result should be quite robust. This result sets the constraint  $M/L_V^{all} < 520 h (M/L_V)^{\odot}$  independently of the X-ray and strong lensing estimates.

## 7. Image deconvolution

The data can also be usefully used to study the immediate environment of the lens, which shows many interesting lensing features. First we deconvolve the Keck  $V$  and  $I$  images using the MCS algorithm (Magain, Courbin & Sohy 1998). Since several individual dithered frames were available, the simultaneous deconvolution capability of the algorithm

can be applied to improve not only the resolution of the images, but also the sampling. A total of four images were used in the  $V$  and  $I$  bands, which allows an effective reduction in the pixel size of the data to  $0''.108$  in the deconvolved combined image compared with the intrinsic instrumental scale of  $0''.215$  per pixel. In principle, the fundamental limitation in resolution is imposed by the Nyquist frequency set by the *adopted* sampling in the deconvolved frame, i.e. 2 pixels FWHM. Since the present images show sharp, high frequency structures, we found it reasonable to limit ourselves to a resolution of 3 pixels FWHM or  $0''.32$  in both bands and avoid to recover spurious high frequency spatial structure too close to the Nyquist limit. Note that this strict adherence of the deconvolution to this fundamental limitation distinguishes the MCS method from other deconvolution procedures where sharp noisy backgrounds are formed, generating spurious structure.

The simultaneous deconvolution of the frames was performed in the same way as in Courbin et al. (1998a,b). The final deconvolved frames are displayed in Fig. 8 together with the stacks of the 4 original images. Given the low galactic latitude of Q2016+112, many stars are available in the immediate vicinity of our target. Accurate PSFs can therefore be constructed for all the images in the stack. The residual maps obtained after deconvolution were satisfactory for all frames in the  $V$  and  $I$  datasets. However, because the central part of the main lensing galaxy (object  $D$ ) is very sharp in the  $I$  band, we choose to model it as a point source plus a diffuse background. This certainly does not mean that the core of the lens is actually a point source, we model it as such to exclude the spurious high spatial frequencies it would otherwise introduce.

The deconvolution procedure returns the astrometry and photometry of the point sources and decomposes the final image into a sum of point sources plus a diffuse background. A major advantage over other deconvolution algorithms is that the resulting deconvolved images allow accurate aperture photometry for the extended objects, free of significant light contamination by bright point sources such as QSOs. This decomposition capability allows us to derive accurate magnitudes for the lensing galaxy, especially in the  $V$  band since it is heavily contaminated by image B at this wavelength.

A summary of the photometry is given in Table 2, including the well resolved bright arc apparent below the two QSO images as discussed further below.

Recent NICMOS2 archival images (ID: 7495, P.I: Falco, E.) are consistent with the above deconvolution in the near-IR, showing very clearly the main arc below the central luminous galaxy, despite the poor point spread function of images taken prior to the refocusing of the instrument, indicating the arc is relatively red. The H band (F160W) image is shown in Fig 9a for comparison. This extended IR feature was also noted by Langston, Fischer, & Aspin 1991 in high quality ground based IR images.

## 8. Lens Model

The lens was originally discovered in the radio, as a close pair of bright flat spectrum sources (Lawrence et al 1984) separated by  $3''$ . These bright radio components,  $A$  and  $B$ , are accurately coincident with optical QSOs (Schneider et al. 1985). A third radio image,  $C$ , (Fig 9a) lies nearby and is resolved with VLBI into 4 knots along a line of only 0.1 arcsec. These knots have a flatter spectrum than  $A$  or  $B$ , so that their relation to the QSO is not clear (Garrett et al. 1994, Heflin et al. 1991, Nair & Garrett 1998). In addition, image  $C$  is coincident with the center of an arc found in  $K$ -band imaging (Langston, Fischer, & Aspin 1991) and clearly confirmed in an HST NICMOS exposure shown in Fig 9a. The optical counterpart of their  $K$ -band arc is clearly seen in our deconvolved images, which show that it is resolved in the radial as well as the tangential direction. The redshift of both the lens and the source were measured by Schneider et al. (1985) to be  $z = 1.01$  and  $z = 3.2$  respectively.

Here we show that the various images are relatively simply related if the lensed QSO and its host galaxy lie close to the caustic of the lens, so that different parts of the source are magnified by different amounts. The lens model is kept as simple as possible. In addition to the usual choice of variables, i.e. position, position-angle, surface-density normalization and mass ellipticity, we also allow the slope of the mass distribution to vary. This is motivated in part by the recent realization that massive objects have central mass profiles which depart from the usual scaling solution (Huang & Broadhurst 1998) becoming flatter in the core than an isothermal model, with a slope  $\gamma < 1$  for the projected surface mass density distribution  $\Sigma(\theta) \propto \theta^{-\gamma}$ . Fig 9b shows our best fit for the lens features. All are easily reconciled in the context of this simple model, provided the slope of the mass distribution is relatively flat ( $\gamma \sim 0.4$ ). The tolerance on the slope is roughly  $\pm 0.1$  depending on the ellipticity. These two parameters can be traded over a limited range and reproduce the location of the three images and the position angle (PA) of the arc. Fixing the ellipticity of the arc to match that of the optical light,  $e = b/a = 0.7$ , requires a slope  $\gamma = 0.37$ . The central position and the PA of the mass distribution for the best fit are consistent with that of the central elliptical galaxy.

The radial extent or thickness of the arc would be greater for a flat profile, where the magnification is given by for a power law, so the fact that object  $C$  is resolved supports a flat central slope, assuming that the source is relatively symmetric. The radio and optical lensing features can be easily reconciled in more detail when the structure of an AGN is considered. If the QSO lies just outside the caustic then only two images of such a small source form in both the optical and the radio. The outer central region of the host galaxy must extend over the caustic so that the arc is a third image but only of the region of the



host projected inside the caustic. This must also be true of the radio emission which lies in the center of the arc; image  $C$  arises naturally in the context of this model from extended radio emission which originates in a region closer to the QSO than most of the optical arc light, but is spatially distinct from the QSO since it must project inside the caustic.

The best fit model magnification of the radio and optical images of the QSO images,  $A$  and  $B$ , is 8.5 and 6 respectively. The magnification of the radio source  $C$  is much greater. Its location in the center of the arc means that this region of the radio emission straddles the caustic generating a high overall magnification of  $\sim 40$  for the 4 knots. The radio emission could arise from within the generally diffuse radio emission typically found in the central kpc of an AGN or may be an image of a jet. This model is most similar to that of Langston, Fischer, & Aspin 1991, requiring the source to sit on the caustic, and quite unlike the multiple component model suggested by Narasimha, Subramanian, & Chitre 1987.

The mass contained within the critical radius is virtually independent of the mass distribution,  $1.6 \pm 0.2 \times 10^{13} h^{-1} M_{\odot}$ , depending somewhat on cosmology through the ratio of source-lens/source distances, due to the relatively high redshift of the lens. Taking into account the luminosity of the central elliptical  $L_V^D = 4.16 \pm 0.21 \times 10^{10} h^{-2} L_{\odot}$ , the above value defines a very robust value of the mass-to-light ratio within the critical radius  $M/L_D = 389_{-45}^{+45} h (M/L_V)_{\odot}$ ,

Interestingly the mass profile advocated by Navarro, Frenk & White (1997) tends to a similar flat slope at the critical radius, when integrated in projection  $\Sigma(\theta) \propto \theta^{-0.3}$ , and normalized to the mass contained within the critical radius, for a reasonable choice of parameters,  $r_s = 100$  kpc and  $d_c = 3000$ . Extrapolating to larger radius using this profile yields a mass  $M = 1.2_{-0.3}^{+0.3} \times 10^{14} h^{-1} M_{\odot}$  within a radius of  $0.2 h^{-1}$  Mpc, assuming circular symmetry, considerably higher than an extrapolation of a purely isothermal profile, which has a steeper slope within this radius. This mass is compatible with the X-ray estimate of H97, and yields a mass-to-light ratio of  $M/L_V = 372_{-94}^{+94} h (M/L_V)_{\odot}$  using our estimate of the cluster luminosity, where the uncertainty in the mass lies mainly with the unknown ellipticity of the mass distribution at large radius.

## 9. Conclusions

We find clear evidence for a distant cluster of galaxies centered on the QSO lens and luminous X-ray source AXJ2019+112. A tight red sequence of galaxies is detected within a radius of  $0.2 h^{-1}$  Mpc of the known  $z = 1.01$  elliptical lensing galaxy, with a color and

slope indicative of a cluster at  $z = 1$ . We estimate the restframe V-band luminosity of the cluster early-types within a  $0.4h^{-1}$  Mpc aperture to be  $L_V^E = 1.6 \pm 0.2 \times 10^{11} h^{-2} L_\odot$  and the luminosity from all galaxy types to be  $L_V \approx 3.2 \times 10^{11} h^{-2} L_\odot$ . This is an order of magnitude larger than the luminosity estimations previously published for this cluster. If we use the X-ray mass estimations of H97 based on the estimated gas temperature, the mass-to-light ratio within  $0.4h^{-1}$  Mpc is  $M/L_V = 224_{-66}^{+95} h(M/L_V)_\odot$ , similar to massive  $z \lesssim 0.5$  clusters. From a weak lensing analysis it can also be established, independently of the X-ray mass estimate, that for an isothermal cluster

$$M/L_V < 520h \left( \frac{\sigma}{1300 \text{ km s}^{-1}} \right)^2 \left( \frac{\beta}{0.2} \right)^{-1} \left( \frac{r}{200 h^{-1} \text{ kpc}} \right) h(M/L_V)_\odot$$

The observation of a radially resolved optical arc in the cluster center and the detailed model fit to this and the two QSO images requires that the core of the mass distribution is much flatter than isothermal. This analysis allows us to set a robust value of the mass-to-light ratio within the critical radius  $M/L_V = 389_{-53}^{+53} h(M/L_V)_\odot$ . The inferred surface mass distribution is very flat,  $\Sigma \propto \theta^{-0.3}$ , and consistent with the Navarro, Frenk & White (1997) profile for reasonable choices of the core radius and central density. An extrapolation of this profile to larger radius yields a mass-to-light ratio  $M/L_V = 372_{-94}^{+94} h(M/L_V)_\odot$  within a  $200h^{-1}$  kpc aperture.

We have reanalyzed the HRI X-ray data and raise the possibility that the X-ray luminosity of the cluster should be significantly revised downward. A clear source of emission is spatially coincident with the cluster center. Two other sources of emission are probably unrelated, but are smoothed together in the map of Hattori et al (1997) comprising 50% of their X-ray flux estimate. Furthermore we cannot exclude the possibility that the lensed QSO makes a significant contribution to the X-ray flux in the center. Higher quality spatially resolved X-ray spectroscopy is needed to understand the relation between the large beam measurement of a hot thermal spectrum by ASCA and the clumpy nature of the higher resolution ROSAT-HRI maps. Deeper HST images would also be of interest in obtaining a better mass estimate for this cluster from weak lensing. Less than a handful of massive clusters are known at  $z \simeq 1$ , none of which have secure measurements of mass.

NB acknowledges a Basque Government postdoctoral fellowship. TJB and NB acknowledge a LTSA grant NASA NAG-3280. F.C. is supported by contracts ARC 94/99-178 “Action de Recherche Concertée de la Communauté Française” and Pôle d’Attraction Interuniversitaire P4/05 (SSTC, Belgium). We thank Doug Finkbeiner for providing the high resolution extinction estimate.

## REFERENCES

- Bahcall, N. A., & Fan, X. 1998, ApJ, 504, 1
- Bartlett, J. G., Blanchard, A., & Barbosa, D. 1998, A&A, 336, 425
- Bertin, E. & Arnouts, S. 1996, A&AS, 117, 393
- Bertin, E., SExtractor User’s manual, 1998
- Burstein, D. & Heiles, C. 1982, AJ, 87, 1165
- Christian, C. A., Adams, M., Barnes, J. V., Hayes, D. S., Siegel, M., Butcher, H., & Mould, J. R. 1985, PASP, 97, 363
- Courbin, F., Lidman, C., Frye, B.L., Magain, P., Broadhurst, T.J., Pahre, M.A., & Djorgovski, S.G. 1998a, ApJ, 499, L119
- Courbin, F., Lidman, C., & Magain, P. 1998b, A&A, 330, 57
- Dickinson, M. 1995, in ASP Conf. Proc. 86, Fresh Views of Elliptical Galaxies, ed. A. Buzzoni, A. Renzini, & A. Serrano (San Francisco: ASP), 283
- Eke, V. R., Cole, S., Frenk, C.S., & Henry, J.P. 1998, submitted to MNRAS, astro-ph/9802350
- Ferreras, I., Benítez, N., & Martínez-Gonzalez, E. 1998, A&A, 333, 43
- Garrett, M. A., Muxlow, T. W. B., Patnaik, A. R., & Walsh, D. 1994, MNRAS, 269, 902
- Garrett, M. A., Porcas, R. W., Nair, S., & Patnaik, A. R. 1996, MNRAS, 279, L7
- Hattori, M., et al. 1997, Nature, 388, 146 (H97)
- Heflin, M. B., Gorenstein, M. V., Lawrence, C. R., & Burke, B. F. 1991, ApJ, 378, 519
- Hoesktra, H., Kuijken, H., Franx, M., & Squires, G. 1998, ApJ, accepted
- Huang, X., & Broadhurst, T., 1998, in preparation
- Jones, M. E. et al 1997, ApJ, 479, L5
- Kaiser, N., & Squires, G. 1994, ApJ, 404, 441
- Kaiser, N., Squires, G., & Broadhurst, T. 1995, ApJ, 449, 460

- Kneib, J.-P., Soucail, G., Jaunsen, A., Hattori, M., Hjorth, J. & Yamada, T., 1998, CFHT Information Bulletin, number 38
- Kneissl, R., Sunyaev, R.A., & White, S.D. 1998, submitted to MNRAS, astro-ph/9801045
- Kodama, T., Arimoto, N., Barger, A. J., & Aragón-Salamanca, A. 1998, A&A, 334, 99
- Langston, G., Fischer, J., & Aspin, C. 1991, AJ, 102, 1253
- Lawrence, C. R., Schneider, D. P., Schmidt, M., Bennett, C. L., Hewitt, J. N., Burke, B. F., Turner, E. L., & Gunn, J. E. 1984, Science, 223, 46
- Luppino, G.A., & Kaiser, N. 1997, ApJ, 475, 20
- Magain, P., Courbin, F., & Sohy, S., 1998, ApJ, 494, 472
- Moorwood, A., Cuby, J.G., & Lidman, C. 1998, ESO Messenger, 91, 9
- Nair, S., & Garrett, M. A. 1997, MNRAS, 284, 58
- Narasimha, D., Subramanian, K., & Chitre, S. M. 1987, ApJ, 315, 434
- Navarro, J. F., Frenk, C. S., & White, S. D. M. 1997, ApJ, 490, 493
- Persson, S. E., Murphy, D. C., Krzeminski, W., Roth, M., & Rieke, M. J. 1998, AJ in press.
- Poggianti, B. M. 1997, A&AS, 122, 399
- Richards, E. A., Fomalont, E.B., Kellermann, K.L., Partridge, R.B., & Windhorst R.A., 1997, AJ, 113, 1475
- Rosati, P., Della Ceca, R., Norman, C., & Giacconi, R. 1998a, ApJ, 492, L21
- Rosati, P., et al. 1998b, in preparation
- Saunders, R., et al. 1997, ApJ, 479, L5
- Smail, I., Ellis, R. S., Dressler, A., Couch, W. J., Oemler, A., J., Sharples, R. M., & Butcher, H. 1997, ApJ, 479, 70 (S97)
- Smail, I., Hogg, D. W., Yan, L., & Cohen, J. G. 1995, ApJ, 449, L105
- Schlegel, D. J., Finkbeiner, D. P., & Davis, M. 1998, ApJ, 500, 525
- Schneider, D. P., Lawrence, C. R., Schmidt, M., Gunn, J. E., Turner, E. L., Burke, B. F., & Dhawan, V. 1985, ApJ, 294, 66

- Schneider, D. P., Gunn, J. E., Turner, E. L., Lawrence, C. R., Hewitt, J. N., Schmidt, M., & Burke, B. F. 1986, AJ, 91, 991
- Schneider, D. P., Gunn, J. E., Turner, E. L., Lawrence, C. R., Schmidt, M., & Burke, B. F. 1987, AJ, 94, 12
- Squires, G., & Kaiser, N. 1996, ApJ, 473, 65
- Squires, G., Kaiser, N., Babul, A., Fahlman, G., Woods, D., Neumann, D. M., & Böhringer, H. 1996, ApJ, 461, 572
- Stanford, S. A., Eisenhardt, P. R., & Dickinson, M. 1998, ApJ, 492, 461
- Stanford, S.A., Elston, R., Eisenhardt, P., Spinrad, H, Stern, D., Dey, A. 1998, AJ, in press, (astro-ph/9709057)

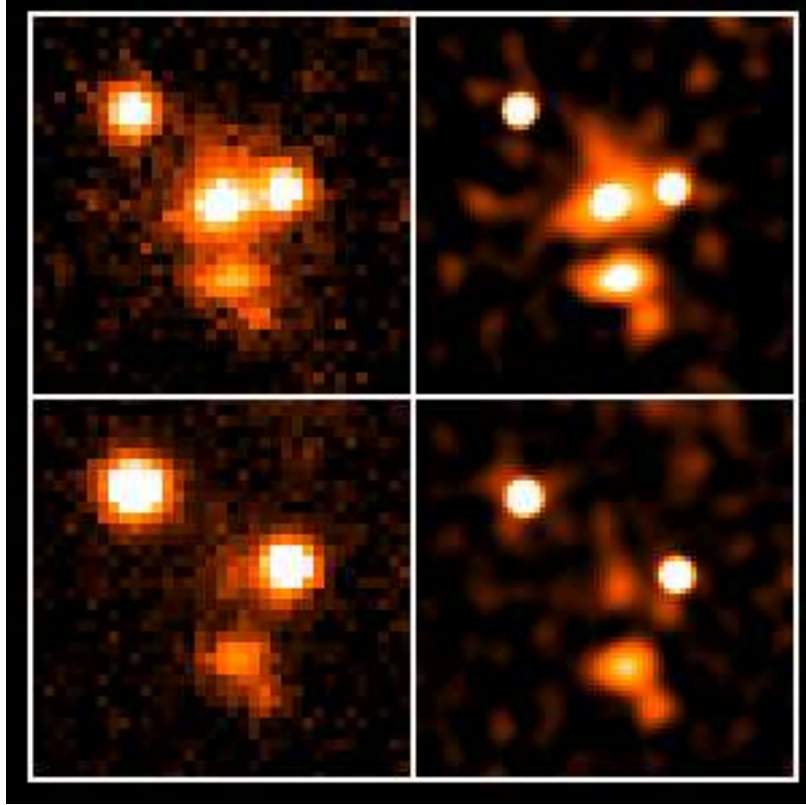


Fig. 8.— (Top) Stack of four  $I$  band Keck/LRIS images of Q2016+112 with a seeing of  $0''.6$  and pixel size of  $0''.215$ . The simultaneous deconvolution of the four frames is shown on the right with a resolution improved to  $0''.32$  and a finer pixel size of  $0''.108$ . (Bottom) Stack of four  $V$  band images and their simultaneous deconvolution. Note the obvious arc feature lying below the two QSO images which modeling shows is an image of the central region of the host galaxy of the QSO. This arc is resolved in both the radial and tangential directions, indicating a flat central potential.

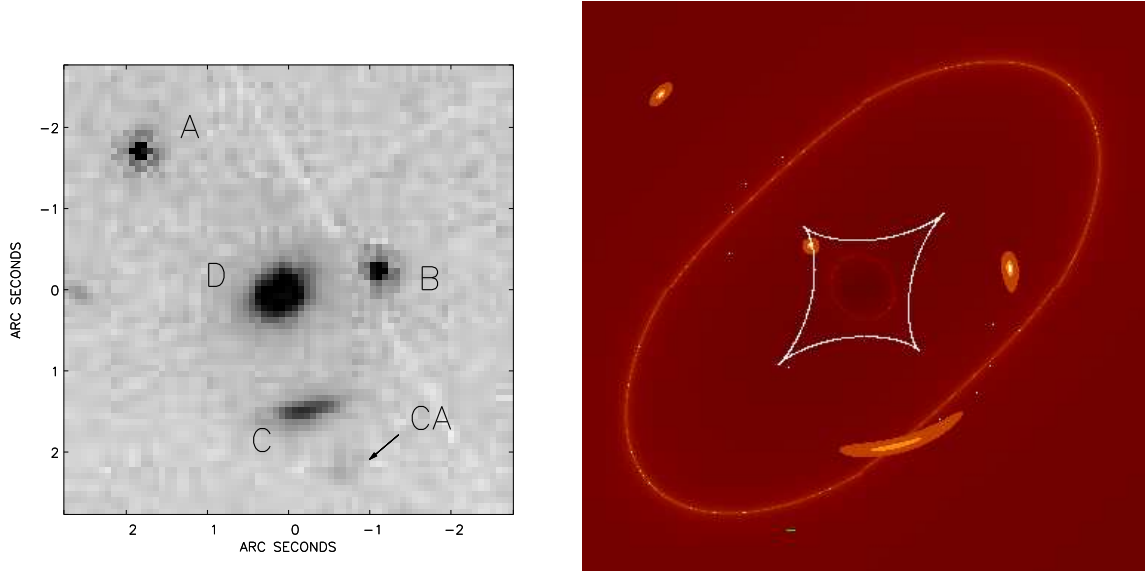


Fig. 9.— The left figure corresponds to the NICMOS H band image of MG 2016+112. To the right, the lens model with the source, critical curve and caustic superposed on the magnification field. The colors of the source represent three regions; the bright central spot indicates the location of the QSO which must lie just outside the caustic generating only two images, and the lower surface brightness region crossing the caustic represents the central host galaxy which forms the optical-IR arc. The center of the arc is coincident with the extended radio source, C, this radio emission maps back to a region of the source immediately inside the caustic, very close but distinct from the central QSO.

Table 1. Cluster sequence candidates

$r''$	$I$	$\delta I$	$V$	$\delta V$	$K_S$	$\delta K_S$	$V - I$	$I - K_S$	$M_V$
00.0	21.20	0.024	24.38	0.06	17.12	0.02	3.17	4.08	-21.89
12.0	23.06	0.072	26.09	0.23	19.31	0.09	3.01	3.75	-20.18
12.2	22.25	0.033	25.40	0.14	19.25	0.06	2.93	3.20	-20.87
14.3	22.92	0.049	25.92	0.23	19.49	0.07	2.99	3.43	-20.35
24.7	21.72	0.024	24.91	0.13	18.17	0.03	3.17	3.55	-21.36
24.8	22.31	0.032	25.39	0.16	19.15	0.06	3.06	2.26	-20.88
25.9	23.54	0.082	26.71	0.28	19.85	0.11	3.14	3.69	-19.56
38.4	23.79	0.095	26.61	0.26	> 21.70	—	2.81	< 2.09	-19.66
39.0	23.63	0.084	26.77	0.30	19.85	0.09	3.12	3.78	-19.50

Table 2. Objects around galaxy D in the I band frame

Object	$I$	$\delta I$	$V$	$\delta V$
A	22.11	0.03	22.10	0.01
B	22.19	0.03	22.56	0.01
C	22.08	0.03	23.46	0.02
CA	22.80	0.06	25.02	0.07
D	21.20	0.02	24.38	0.05